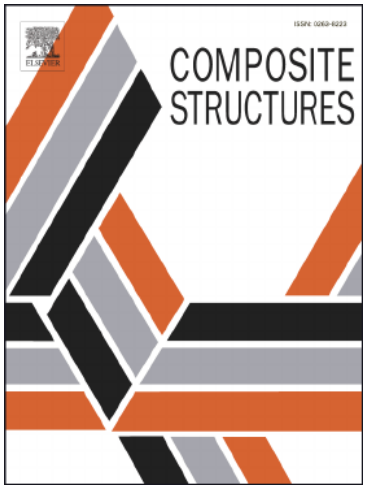

A Plate Model for Compressive Strength Prediction of Delaminated Composites

Rizwan S. Choudhry, Andrew T. Rhead, Mark W.D. Nielsen, Richard Butler

PII: S0263-8223(18)31892-0
DOI: https://doi.org/10.1016/j.compstruct.2018.11.066
Reference: COST 10431

To appear in: *Composite Structures*

Received Date: 19 June 2018
Revised Date: 12 October 2018
Accepted Date: 23 November 2018

Please cite this article as: Choudhry, R.S., Rhead, A.T., Nielsen, M.W.D., Butler, R., A Plate Model for Compressive Strength Prediction of Delaminated Composites, *Composite Structures* (2018), doi: https://doi.org/10.1016/j.compstruct.2018.11.066

A Plate Model for Compressive Strength Prediction of Delaminated Composites

Rizwan S. Choudhry[1,2], Andrew T. Rhead[2], Mark W.D. Nielsen[2] & Richard Butler[2]*

[1]*Department of Mechanical Engineering and Built Environment, College of Engineering, University of Derby, Derby, UK*
[2]*Department of Mechanical Engineering, University of Bath, Bath, UK*
**corresponding author: R.Butler@bath.ac.uk*

Abstract

Damage tolerance is of critical importance to laminated composite structures. In this paper, we present a new semi-analytical method for predicting the strain at which delamination propagation will initiate following sublaminate buckling. The method uses a numerical strip model to determine the thin-film buckling strain of an anisotropic sub-laminate created by delamination, before evaluating the strain energy release rate for delamination propagation. The formulation assumes that all energy is available for propagation in a peeling mode (Mode I); avoiding an approximate mixed-mode criterion. Results are compared with twelve experimentally obtained propagations strains, covering a variety of laminates each containing a circular PTFE delamination. Comparison shows agreement to within 12% for balanced sublaminate tests in which delamination propagation occurred before intra-ply cracking. The method can be used to significantly improve the damage tolerance of laminates, opening up new opportunities for structural efficiency using elastic tailoring, non-standard ply angles and material optimisation.

Keywords: damage tolerance; delamination; CAI; modelling; impact; buckling

1 Introducon

Aerospace engineers are always in search of design tools that help them reliably and quickly achieve mass and cost savings by reducing the extent of overdesign, which is often a consequence of lack of confidence in the accuracy of predictive models. This is particularly true for aerospace structures where material innovations in carbon fibre reinforced laminates theoretically allow for significant mass savings. However, their true potential is often difficult to realize in practice, because of vulnerability to barely visible impact damage (BVID). In the absence of adequate design methodologies, conservative strain limits can lead to component strengths that are less than half of the equivalent value of aluminium [1].

The topic of barely visible impact damage and its influence on compression after impact (CAI) strength has received significant attention from the composites research community. Despite this significant volume of research there is little for the designer to use in terms of an actual theory that allows reliable and robust design for CAI strength. A few analytical studies have been conducted [2-5]. However, most articles focus on either: (i) experimental evaluation of the damage mechanisms (see for example [6–8]) or (ii) high fidelity Finite Element modelling and comparison with experiments (see for example [9–12]). While these papers present important analysis techniques and results, they do not equip the designer with a cost effective tool to solve the design problem. In particular, we note that although FE analysis using high fidelity cohesive elements and non-linear dynamic analysis [9–11] can be used reliably for detailed analysis and bench marking for a particular problem, the associated computational and model setup cost make it unsuitable for design. Thus, this paper aims to address this gap in understanding by presenting a semi-analytical methodology to predict CAI strength suitable for design use.

We consider the compressive loading of a laminate with a sub-surface delamination. Critical delamination typically occurs at a below surface depth of 10 to 20% of laminate thickness due to low velocity and low energy in-service impact on composite structures [13]. Other damage mechanisms such as transverse micro-cracking may also occur but these are structurally less harmful for compression panels and are thus ignored in this model. Under compressive loading the thin sub-laminate caused by delamination tends to buckle and form a blister. It has been established through experiments (e.g. [14–17]) that sufficient structural integrity is retained until the blister starts to grow, which happens when the underlying delamination grows. The model presented in this paper predicts the strain required for the growth of delamination (threshold strain) by comparing the elastic strain energy released when the post buckled sub-laminate grows, with the Strain Energy Release Rate (SERR) required to extend the crack. Unlike our previous 1-dimensional model [14,18,19], the new model uses the full 2-dimensional form of the strain energy equation and applies it to elliptical propagation. This factor plays a significant role in predicting the threshold strain for some cases and results in a model which is simple to implement and can quickly and reliably generate a threshold

strain for designing structures that have been subjected to BVID and are expected to operate primarily under compression but with any (general) combination of bi-axial strain.

Past analytical studies [2-5] use thin-film modelling assumptions, which ignore any effect of the sublaminate buckling on the full laminate. This assumption is considered to be appropriate when (i) sublaminates are 10-20% of full laminate thickness, and (ii) full laminates do not buckle. Chai & Babcock presented an analytical method for propagation of a delamination in an isotropic strut [2] giving a total SERR to compare with a Mode I fracture criterion. They later extended this technique to a method for an elliptical delamination in an orthotropic plate using a Rayleigh-Ritz approach to produce the out-plane displacements [3]. This was covered by Hutchinson and Suo's comprehensive review [4]. Flanagan [5] produced an identical 2D physical model to Chai and Babcock but simplified the approximations with the use of an integrated SERR around the crack front. Whitcomb showed that the ratio of Mode I to Mode II SERR components decreases with increasing load above buckling as well as initial imperfection (buckling amplitude) for a simple 1D case of sublaminate buckling using thin-film solutions for the post-buckle with FEA to analyse the crack tip [20], confirming the complexity of mode-mixity in post-buckling. Hutchinson and Suo [4] found the same effect with increasing strain above buckling. All of these analytical models generally assume: idealised damage (strut, circle or ellipse); a thin-film boundary condition; and crack growth on a continuous front instead of at a localised node. Simplifications of the full mechanics of the physical problem are applied in such models.

The aim of this paper is to capture the critical behaviour effecting the CAI strength of composite laminates and aid design. The model is created to produce a reliable and conservative approach to design. The unique features of the model are that accurate and efficient buckling calculations are conducted using VICONOPT [21] software; bending energy is evaluated assuming that no post-buckled stiffness is developed in the sublaminate, exaggerating the Mode I bending energy available for propagation. The model is applicable to all loadings and non-standard angle designs; it compares a (predominately) conservative total SERR to a critical Mode I fracture toughness of the resin material. However it does not account for all forms of stiffness coupling. The complexity of impact damage is likely to provide mechanics that bypass assumptions of most models, nevertheless it is prudent to take a conservative outlook of such complexities especially with new laminate design concepts, such as use of non-standard ply angles.

In the following sections we present the methodology which combines an analytical strain energy formulation with a numerical method for buckling analysis. A set of experimental results are then compared with predictions of this semi-analytical method.

2 The post buckling delaminaon propagaon model

2.1 Model derivaon

We consider thin-film buckling of the sub-laminate created by an assumed circular region of delamination within a laminated plate. A general 2D deformation scenario is assumed to exist within the laminate where there is compatibility of strains at the laminate/sub-laminate boundary, these strains are also applied to the sub-laminate. We assume that the deformation of the laminate/sub-laminate remains purely elastic until the delamination starts to grow by propagation along the elliptical boundary, see Fig. 1(a). The energy, for propagation of the ellipse, arises from: (i) the reduction in membrane energy between unbuckled and buckled states and (ii) the reduction in bending energy as the sub-laminate buckle relaxes. We assume that bending energy is simply the product of post-buckled end shortening and buckling load [22]. Our assumption neglects any post-buckled stiffness which will occur in practice, as a result of local stress variation in the sub-laminate. A general strain state is converted to principal strains, removing shear strain from the problem. These assumptions eliminate the need for a mixed mode finite element formulation, involving variation in peeling, shearing and tearing forces along the delamination boundary. Instead, all of the energy is accumulated in bending the thin film (without any post-buckled stiffness) and released in

Mode I fracture. The use of this equivalent energy approach simplifies the formulation and leads to results which compare well with experimental tests as shown later.

The energy difference between the energy in the unbuckled sub-laminate and post-buckled sub-laminate over the elliptical area A, see Fig. 1 (b), is given by

$$U = \int_0^A (U_M - (U'_M + U'_B))\, dA \tag{1}$$

where, U_M is the membrane energy in the unbuckled sub-laminate, U'_M and U'_B are the membrane and bending energies in the post-buckled sub-laminate.

In order to model propagation, we assume that growth can occur in a or b directions in Fig. 1(a). The post-buckled bending energy is assumed to be similar to that of a strut, being the product of post-buckled end-shortening and buckling load with no post-buckled stiffness ([22], page 171). Hence

$$\int_0^A U'_B\, dA = \int_0^A \left(\{\varepsilon^c\}^T [A_{sl}](\{\varepsilon\} - \{\varepsilon^c\})\right) dA$$
$$= \pi ab \{\varepsilon^c\}^T [A_{sl}](\{\varepsilon\} - \{\varepsilon^c\}) \tag{2}$$

$\{\varepsilon^c\}$ is the vector of principal applied strain at buckling for the first sub-laminate buckling mode and the applied strain $\{\varepsilon\}$ is a factor F of the buckling strain;

$$\{\varepsilon^c\} = \begin{Bmatrix} \varepsilon_x^c \\ \varepsilon_y^c \\ 0 \end{Bmatrix} \text{ and } \{\varepsilon\} = F\{\varepsilon^c\}, \text{ where } F > 1 \tag{3}$$

$[A_{sl}]$ is the membrane stiffness matrix of the sub-laminate as defined using classical lamination theory (CLT).

$$[A_{sl}] = \begin{bmatrix} A_{11} & A_{12} & A_{13} \\ A_{12} & A_{22} & A_{23} \\ A_{31} & A_{32} & A_{33} \end{bmatrix}_{sl} \tag{4}$$

If we represent buckling using the following approximations

$$\{\varepsilon^c\} = \frac{K_1}{a^2}\{\bar{\varepsilon}\} \qquad a$$

and

$$\{\varepsilon^c\} = \frac{K_2}{b^2}\{\bar{\varepsilon}\} \qquad \text{for growth in } b \tag{5}$$

where K_1 and K_2 are buckling coefficients and $\{\bar{\varepsilon}\}$ is the vector of principal applied strain before buckling;

$$\{\bar{\varepsilon}\} = \begin{Bmatrix} \bar{\varepsilon}_x \\ \bar{\varepsilon}_y \\ 0 \end{Bmatrix} \tag{6}$$

Assuming growth in b and substituting Eq. (5) in Eq. (2) we have

$$U_B' = \pi a \frac{K_2}{b} \{\bar{\varepsilon}\}^T [A_{sl}] \left(\{\varepsilon\} - \frac{K_2}{b^2} \{\bar{\varepsilon}\} \right) \tag{7}$$

The energy release rate for growth in b is

$$-\frac{\partial U_B'}{\partial b} = \pi a \frac{K_2}{b^2} \{\bar{\varepsilon}\}^T [A_{sl}] \left(\{\varepsilon\} - \frac{3K_2}{b^2} \{\bar{\varepsilon}\} \right) \tag{8}$$

The difference in the unbuckled (U_M) and post-buckled (U_M') membrane energy from Eq. (1) is given by

$$\begin{aligned} U_M^* &= \int_0^A (U_M - U_M') dA \\ &= \frac{\pi ab}{2} \left(\{\varepsilon\}^T [A_{sl}] \{\varepsilon\} - \{\varepsilon^c\}^T [A_{sl}] \{\varepsilon^c\} \right) \\ &= \frac{\pi ab}{2} \left(\{\varepsilon\}^T [A_{sl}] \{\varepsilon\} - \frac{K_2^2}{b^4} \{\bar{\varepsilon}\}^T [A_{sl}] \{\bar{\varepsilon}\} \right) \end{aligned} \tag{9}$$

Then

$$\frac{\partial U_M^*}{\partial b} = \frac{\pi a}{2} \left(\{\varepsilon\}^T [A_{sl}] \{\varepsilon\} + \frac{3{K_2}^2}{b^4} \{\bar{\varepsilon}\}^T [A_{sl}] \{\bar{\varepsilon}\} \right) \tag{10}$$

The total strain energy release rate with growth in b is

$$\begin{aligned} \frac{\partial U}{\partial b} &= \frac{\partial U_M^*}{\partial b} - \frac{\partial U_B'}{\partial b} \\ &= \frac{\pi a}{2} \left(\{\varepsilon\}^T [A_{sl}] \{\varepsilon\} + \frac{3{K_2}^2}{b^4} \{\bar{\varepsilon}\}^T [A_{sl}] \{\bar{\varepsilon}\} + \frac{2K_2}{b^2} \{\bar{\varepsilon}\}^T [A_{sl}] \{\varepsilon\} - \frac{6K_2^2}{b^4} \{\bar{\varepsilon}\}^T [A_{sl}] \{\bar{\varepsilon}\} \right) \\ &= \frac{\pi a}{2} \left(\{\varepsilon\}^T [A_{sl}] \{\varepsilon\} - 3\{\varepsilon^c\}^T [A_{sl}] \{\varepsilon^c\} + 2\{\varepsilon^c\}^T [A_{sl}] \{\varepsilon\} \right) \\ &= \frac{\pi a}{2} \left(\{\varepsilon\}^T - \{\varepsilon^c\}^T \right) [A_{sl}] \left(\{\varepsilon\} + 3\{\varepsilon^c\} \right) \end{aligned} \tag{11}$$

Using Eq. (3), we re-write Eq. (11) as

$$\frac{\partial U}{\partial b} = \frac{\pi a}{2}(F-1)(F+3)\{\varepsilon^c\}^T[A_{sl}]\{\varepsilon^c\} = \pi a\bar{U} \tag{12}$$

A similar expression can be created for growth in a

$$\frac{\partial U}{\partial a} = \frac{\pi b}{2}(F-1)(F+3)\{\varepsilon^c\}^T[A_{sl}]\{\varepsilon^c\} = \pi b\bar{U} \tag{13}$$

where

$$\bar{U} = \frac{1}{2}(F-1)(F+3)\{\varepsilon^c\}^T[A_{sl}]\{\varepsilon^c\} \tag{14}$$

Propagation occurs when the energy released, dU, by a small new area of delamination, dA, is equal to the critical value of Mode I strain energy release rate for the material G_{IC}. Considering the symmetric delamination growth in Fig. 1(a), where the change in total elliptical energy dU is utilized in growing two crack fronts simultaneously i.e. energy dU is released at either edge of the ellipse as it grows by dA in both directions along its major axis we can write

$$\frac{dU}{dA} = \frac{G_{IC}}{2} \tag{15}$$

Introducing the Leibniz notation for the chain rule produces;

$$\begin{aligned} \frac{dU}{dA} &= \frac{\partial U}{\partial b}\frac{db}{dA} && \text{for growth in } b \\ \frac{dU}{dA} &= \frac{\partial U}{\partial a}\frac{da}{dA} && \text{for growth in } a \end{aligned} \tag{16}$$

In order to determine dA, in Eq. (16) consider the schematic representations shown in Fig. 1(a). Once the applied strain reaches the threshold strain, the delamination boundary grows along either the axis b by an amount db (or along axis a by an amount da). It is not known *a priori* if the crack growth will occur along a or b but growth occurs along the path that results in the minimum value of threshold strain. Thus, for the case in Fig. 1(a) where growth occurs along b, the rate of change in length b with total crack area ($A = \pi ab$) may therefore be formulated as follows.

$$\begin{aligned} \frac{db}{dA} &= \frac{1}{\pi a} && \text{for growth in } a \\ \frac{da}{dA} &= \frac{1}{\pi b} && \text{for growth in } b \end{aligned} \tag{17}$$

Substituting Eqs. (12), (13), (15) and (17) into (16) we get the following condition for propagation;

$$2\bar{U} \geq G_{IC} \tag{18}$$

Substituting the definition of $\bar{U}$ from Eq. (14) in Eq. (18), and considering only the initiation of crack propagation, where, F_{th} represents the threshold value of load factor F, we get;

$$\left(F_{th}^2 + 2F_{th} - 3\right)\left\{\left(A_{11_{sl}}\varepsilon_x^c + A_{21_{sl}}\varepsilon_y^c\right)\varepsilon_x^c + \left(A_{12_{sl}}\varepsilon_x^c + A_{22_{sl}}\varepsilon_y^c\right)\varepsilon_y^c\right\} = G_{IC} \tag{19}$$

Equation (19) may be simplified as;

$$\left(F_{th}^2 + 2F_{th} - 3\right) u_T = G_{IC} \tag{20}$$

where u_T is the in-plane energy in terms of principal buckling strains from Eq. (19). The quadratic equation (20) can be readily solved for F_{th} with roots and noting that compressive strains are positive and $F_{th} > 1$ for the post buckling response, we get;

$$F_{th} = \left(\sqrt{4 + \frac{G_{IC}}{u_T}} - 1\right) \tag{21}$$

Thus using the definition of F_{th}, from Eq. (3), we may rewrite Eq. (21) in terms of the applied strain ε_x as below,

$$\varepsilon_x^{th} = \varepsilon_x^C\left(\sqrt{4 + \frac{G_{IC}}{u_T}} - 1\right) \tag{22}$$

2.2 Buckling Analysis

In the above expression, in addition to the material properties, the buckling strain vector $\{\varepsilon^c\}$ needs to be known *a priori*. Buckling analysis can be readily conducted using either an FE based eigenvalue solver or using some other method. In this paper, the finite strip program VICONOPT [21] is used, since this is a computationally efficient and easy to implement method suitable for parametric optimization and evaluation of multiple design scenarios [23–26]. For panels and loadings that are prismatic in the x direction, VICONOPT provides periodic solutions to the equilibrium equation that governs buckling;

$$\begin{aligned} D_{11}\frac{\partial^4 w}{\partial x^4} + 4D_{26}\frac{\partial^4 w}{\partial x \partial y^3} + 2(D_{12} + 2\,D_{66})\frac{\partial^4 w}{\partial x^2 \partial y^2} + 4D_{16}\frac{\partial^4 w}{\partial x^3 \partial y} + D_{22}\frac{\partial^4 w}{\partial y^4} \\ + \left(N_x\frac{\partial^2 w}{\partial x^2} + 2N_{xy}\frac{\partial^2 w}{\partial x \partial y} + N_y\frac{\partial^2 w}{\partial y^2}\right) = 0 \end{aligned} \tag{23}$$

where N_x , N_y and N_{xy} are in-plane forces and D_{11}, D_{12}, D_{22}, D_{16} and D_{66} are the bending stiffness terms of classical lamination theory, and w is out-of-plane displacement. Equation (23) assumes that there is no coupling between the in-plane and out-of-plane deformation, i.e. no $[B]$ matrix. This assumption is true only for symmetric laminates, therefore in order to analyse non-symmetric layups VICONOPT defines an effective $[D]$ matrix that correctly directly relates moments and curvatures for these cases ([27], page 33);

$$[D]_e = [D] - [B]^T[A]^{-1}[B] \quad (24)$$

Hence, the terms of $[D]_e$ are used instead of $[D]$ in Eq. (23). The solution of this equation is via exact, periodic functions [28] of the form:

$$w = f_1(y)\cos\frac{\pi x}{\lambda} - f_2(y)\sin\frac{\pi x}{\lambda} \quad (25)$$

where $f_1(y)$ and $f_2(y)$ allow various boundary conditions to be applied on the longitudinal edges of panels, including free, simple, clamped and elastic supports.

The delamination considered in this case is circular and the sub-laminates are either two or three layers thick with various ply orientations given in Table 1. VICONOPT divides the circular sub-laminate into a series of connected strips across its width where conditions of compatibility and equilibrium are satisfied along strip boundaries (node-lines). The half-wavelengths λ in Eq. (25) are defined by the radius of the elliptical sub-laminate $2a$ (see Fig. 1) divided by the number of half-wavelengths assumed along this length. The clamped boundary assumed around the perimeter of the circular delamination is represented using VICONOPT point supports [29] positioned around the circular circumference of the delamination and along the node-line of each strip. Buckling modes are constrained at these points, and so the continuous boundary is approximated by this series of point supports, shown as crosses in Fig. 2 (right). We assume that the extent of the delaminated region is approximated by points at ten degree intervals around the circle (i.e. 18 strips, 19 node lines and 36 point supports to represent the circular sub-laminate, see Fig. 2(right)). VICONOPT finds the mode of minimum energy, satisfying the boundary conditions applied at the point supports [29].

In VICONOPT, buckling loading factors are derived through an eigenvalue analysis which is executed on the transcendental stiffness matrix derived from the solution of the governing differential of the constituent strips, Eq. (23). The transcendental eigenvalue problem requires an iterative solution that is performed using the Wittrick-Williams algorithm [30]. The lowest buckling load found for a range of values of is taken as the critical buckling strain for the sub-laminate. A sensitivity analysis was carried out to establish that the number of strips used was sufficient to accurately determine the buckling strain and mode shapes, indicating convergence using 18 strips.

Thermal curing stresses may become important when the sub-laminate is not balanced. Thus in each case the thermal curing loads were calculated by applying a thermal cooling step from the curing temperature of 180°C to room temperature of 20°C. The normal and shear stresses on each ply within the sub-laminate were calculated and converted into equivalent line loads (shell edge loads) by multiplying these components with the thickness of the ply. These were then integrated over the total number of sub-laminate plies to determine the thermal curing load due to residual stresses. The edge loads obtained were applied as dead load inputs to the VICONOPT analysis file. The critical values of buckling strain, ε_x^c and ε_y^c, and the buckling mode shapes were obtained from the VICONOPT analysis. These values were then used in Eq. (22) to determine the threshold strain.

3. Experimental validaon

The model presented in this paper has been validated experimentally using, previously published [14,17] and unpublished data. All experimental compression tests were carried out on specially designed compression coupons that had a circular delamination, which was induced artificially during coupon manufacture. Coupons were constructed using unidirectional 0.25mm Hexcel T700GC/M21 pre-preg with material properties, E_{11} = 136 GPa, E_{22} = 8.9 GPa, G_{12} = 4.5 GPa, $_{12}$ = 0.35, $\alpha_{11} = -1.0 \times 10^{-6}/°C$, $\alpha_{22} = 25.8 \times 10^{-6}/°C$ and G_{IC} = 550 J/m^2. A range of stacking sequences (Table 1) were used to

demonstrate the applicability of model. The specimens were hand laid, vacuum bagged and cured at 180 °C. The delamination was induced during the layup process by placing a 39mm diameter, 0.0125 mm thick, circular Teflon ™ (Polytetrafluoroethylene) insert in the mid (x-y) location of the coupon. The insert was placed either two or three plies below the surface, depending on the layup (see Table 1). This insert prevented bonding between the sub-laminate and laminate layers in the circular region. The depth and diameter of the delaminating insert were chosen to reflect the typically observed limits of BVID in composite aerospace structures. The compression coupons had an average length of 210 mm, width of 100 mm, and a thickness of 4 mm. The details of all the laminates and sub-laminate combinations evaluated for model validation are provided in Table 1.

Sub-laminate	Laminate (delamination indicated by //)	Source
0_2/90	[0_2/90//45/-45/45/-45/90/90/-45/45/-45/45/90/0_2]	[14]
0_2	[0_2//45/-45/90/45/-45/90/90/-45/45/90/-45/45/0_2]	[14]
15/30	[15/30//-30/-15/0/90/90/0/0/90/90/0/-15/-30/30/15]	New
0/90_2	[0/90_2//45/-45/45/-45/0/0/-45/45/-45/45/90_2/0]	[14]
90/0/90	[90/0/90//45/-45/45/-45/0/0/-45/45/-45/45/90/0/90]	[14]
90_2/0	[90_2/0//45/-45/45/-45/0/0/-45/45/-45/45/0/90_2]	[14]
0/45	[0/45//0/-45/90/45/-45/90/90/-45/45/90/-45/0/45/0]	[14]
15/60	[15/60//-60/-15/0/90/90/0/0/90/90/0/-15/-60/60/15]	New
±30	[30/-30//0/90_2/0/90/0/0/90/0/90_2/0/-30/30]	[17]
(±30)NS	[30/-30//0_2/±30/30/-+60/±30/30/0_2/-30/30]	[17]
45_2	[45_2//-45_2/90/0/90/0/0/90/0/90/-45_2/45_2]	[14]
±45	[45/-45//0_2/-45/90/+45/90/90/+45/90/-45/0_2/-45/45]	[14]

Table 1: Layup of laminates and sub-laminates for test cases used for model validation.

The compressive load was applied in displacement control in a Universal Testing Machine (UTM) using a compression rig with anti-buckling guides at a displacement rate of 0.1 mm/min. The anti-buckling guide has a circular window which allows sub-laminate buckling but restricts laminate buckling. The experimental setup ensures that the laminate is under uni-axial compressive strain, ε_x and the transverse boundary is free. Thus, there is no shear strain and the assumed transverse strain is:

$$\varepsilon_y = -\nu_L \varepsilon_x \tag{26}$$

where ν_L is the Poisson's ratio of the laminate.

The displacement and strain field were measured using a Limess Digital Image Correlation (DIC) system employing a stereo pair of 1MP high speed Photron SA3 Cameras. Post-processing was undertaken using commercially available software VIC3D (by Correlated Solutions). Far field strains were also recorded using strain gauges mounted on either side of the coupon. The DIC and strain gauge data was used in support of each other to determine the threshold strain. Further details of the procedure can be read from [14,17].

4. Results

A summary of sub-laminate buckling and threshold strains from the model (Eq. (22)) and experiments for all laminates of Table 1 are given in Table 2. Percentage difference comparisons of the Plate model threshold predictions to the experimental values are given for both G_{IC} = 550 J/m^2 [31] and G_{IC} = 331 J/m^2 [32], values seen in the literature. Figure 3 presents the threshold data in graphical form for Strip [14] and Plate model comparisons to experiment. The values of ^{c} in Table 2 as well as $_{th}$ for the Strip model in Fig. 3 are slightly different from the values presented in [14,17]. This is because the new analysis accounts for the curing residual stresses in the model (see section 2.3). Figure 4 shows FEA threshold results presented previously [14,17] compared to experimental values. The FEA used material properties of G_{IC} = 550 J/m^2 G_{IIC} = 1550 J/m^2 G_{IIIC} = 1550 J/m^2 and an $\eta = 1.75$ in the Benzeggagh–Kenane law to predict the

point of crack initiation/propagation, see Eq. (27). Mode II and III properties were supplied by the Hexcel Corporation. See [14] for more details on the FEA.

$$G_{TC} = G_{IC} + (G_{IIC} - G_{IC})\left(\frac{G_{II} + G_{III}}{G_I + G_{II} + G_{III}}\right)^{\eta} \quad (27)$$

Figure 2 illustrates the alignment of the ellipse for the 0/45 sub-laminate for both experimental (DIC) and VICONOPT mode shape results. Figures 5 and 6 show load vs. strain data for the (new) experimental tests on the 15/60 and 15/30 sub-laminates, respectively. Insets show the sequence of events during loading as captured by DIC. Point (i) in Figure 6 for the 15/30 sub-laminate indicates the occurrence of intra-ply cracking in the surface ply before propagation of the delamination beyond the original area at point (ii). Delamination is deemed to have occurred once the buckled region spreads outside of the boundary of the original delaminated area which is indicated by a white circle in Figs. 5 and 6. The experimental threshold strain is calculated as the average strain of all strain gauges at this instant. Figure 7 shows intra-ply cracks in the surface plies of the 0_2, 45_2 and 15/30 sub-laminates. For clarity, images for the 45_2 and 15/30 sub-laminates are at load points significantly higher than the load at which propagation outside of the originally delaminated region occurred. However, for each of the 0_2, 45_2 and 15/30 sub-laminates intra-ply cracking of surface plies preceded propagation of delamination e.g. contrast insets (b) and (c) in Figure 6.

Sub-laminate	ε_x^C VICONOPT	ε_x^C Experiment	ε_x^{th} FEA init.	ε_x^{th} Experiment	ε_x^{th} Plate model G_{IC} = 550 J/m^2	ε_x^{th} Plate model G_{IC} = 331 J/m^2	Plate model vs Exp. Diff. (%)**	
							G_{IC} = 550 J/m^2	G_{IC} = 331 J/m^2
0_2/90	1260	1060	2838	2650	2463	2037	-7%	-23%
0_2	648	1250	3583	3540*	2477	1910	-30%*	-46%*
15/30	758	1350	-	4490*	2995	2306	-33%*	-49%*
0/90_2	2430	2340	3806	4280–3700	3568	3142	-4%	-15%
90/0/90	2270	2630	3655	4260–3950	3474	3028	-12%	-23%
90_2/0	2430	2800	3811	3730	3568	3142	-4%	-16%
0/45	473	400	3035	2700–2500	3338	2543	34%	2%
15/60	601	1450	-	3030	3703	2823	22%	-7%
±30	439	1000	4895	3600	3494	2662	-3%	-26%
(±30)NS	587	1700	5535	4150	4195	3196	1%	-23%
45_2	1730	1200	7862	7050–6310*	5685	4423	-10%*	-30%*
±45	793	3010	7350	6700	5970	4548	-11%	-32%

* Intra-ply cracking occurred in the buckled surface plies prior to delamination propagation
** % difference are for lower experimental values
Table 2: Comparison of experimental threshold strains with threshold strain prediction using FEA analysis [14,17] and the new Plate model (Eq. (22)) for G_{IC} = 550 J/m^2 and G_{IC} = 331 J/m^2.

5. Discussion

Comparison of experimental and VICONOPT sub-laminate buckling strain results in Table 2 shows VICONOPT predictions are typically conservative. Large differences are the result of adhesion between the sub-laminate and Teflon insert as has previously been discussed [14,17]. In contrast this behaviour has been concluded to be insignificant as no difference was found when drilling a hole through the base laminate to remove any effects of an enclosed vacuum [33]. Other differences are a consequence of the out-of-plane deformation of sub-laminates with extension-twist coupling (15/30, 15/60, ±30, $(\pm30)_{NS}$, ±45), causing the sub-laminate mode shape to contact with the parent laminate from the start of loading; a non-linear effect not dealt with in VICONOPT buckling analysis. However, once the buckling mode shape stabilises, as demonstrated in Figure 6, predicted buckling mode shapes are in agreement with experiments with regard to shape and alignment of major ellipse axes, see Figure 2.

The value of G_{IC} for T700GC/M21 has been found to vary in the literature and so Plate model threshold predictions and percentage difference to experiment are both included in Table 2 for G_{IC} = 550 J/m^2 [31]

and G_{IC} = 331 J/m^2 [32], to show the effect of this variation. Only results for G_{IC} = 550 J/m^2 are shown in Fig. 3 for the Plate and Strip model predictions and Fig. 4 for the FEA predictions from past papers. This larger value has provided accurate match to experiments when used in the model as well as FEA [14,17], and thus is kept for predictive purposes. Despite this, the value of G_{IC} = 331 J/m^2 has been proposed [32] via monitoring the applied loading and opening displacement in a single DCB test. A conservative reduction method, modified beam theory, was used to back calculate values of G_{IC} at each stage of the crack length throughout the test, seeing a standard deviation of ±19.2 J/m^2. Doubt is cast on this value because using the same reduction method for G_{IIC} produced a massively conservative value of 443 J/m^2 (SD = 283 J/m^2) compared to 1550 J/m^2, given by the manufacturer, and 1387 J/m^2 seen in [31]. Others have found G_{IC} values between 450-700 J/m^2 by equating the propagation load and/or displacement of analytical and FE methods with values prescribed by a standard DCB experiment [34]. The effect of this lower G_{IC} value can be seen in Table 2 and predictions can be anywhere from 11.9-23.1% lower depending on the sublaminate stack. This lower value makes nearly all predictions conservative except for the 2% over conservatism for the 0/45 sublaminate. Large conservatism in design scenarios is potentially problematic if the model under predicts the point of failure by around 40% using this value of G_{IC} (see Table 2). Therefore it is important to use the correct values of fracture toughness properties in delamination growth prediction models to produce designs that are not massively overdesigned.

Post-buckling of the sub-laminate with increasing compressive loading in some cases leads to intra-ply cracking in surface plies prior to propagation outside the initially delaminated area; contrast DIC images (d) and (e) in Fig. 5 and (c) and (d) in Fig. 6. This is caused by bending stresses in the buckle resulting in tension and shear in the resin, leading to failure. Intra-ply cracking relieves stresses in the buckled sub-laminate, reducing energy available for propagation thus increasing the threshold strain. Analysis of results in Table 2 and Figure 3 shows that significant differences in experimental and predicted Plate model threshold strains occur for 0_2, 45_2 and 15/30 laminates. It is assumed that this is a consequence of intra-ply cracking as shown in Figure 7. In such cases the one-dimensional formulation of the threshold strain in [14,17] is more appropriate, see Figure 3. The 1D formulation does not contain contributions to the energy for propagation from Poisson's ratio and transverse strains which is consistent with the effect of the intra-ply crack. The delaminations here propagate in the fibre directions and not necessarily transverse to the load as would be typically seen for uncracked sublaminates [35], e.g. the 0/0 sublaminate propagates in the fibre/load direction. Results from the 1D formulation are within 8% of experimental results in cases where intra-ply cracks have formed in the buckled sub-laminate, see Table 2 and Fig. 3. However, realistic impact events occurring during the service life of composite structures produce delamination at multiple interfaces and hence sub-laminates of varying and multiple thicknesses. As intra-ply cracking increases propagation strains for thin sub-laminates, propagation under compressive loading is likely to occur at deeper interfaces (i.e.10-20% of laminate thickness) where such ply cracking is less likely to relieve stresses.

FEA threshold predictions from previous papers [14,17] are also shown in Table 2 and Figure 4, since they account for the full post-buckling effects and mode-mixity at the crack front. FEA results correlate well with experiments except for cases where there is a large amount of extension-twist coupling causing sublaminate/laminate contact (±30 and $(\pm 30)_{NS}$) or where the behaviour is dominated by intra-ply cracking (45_2), as neither are accounted for in the FEA model. The 1D model matches the 0/0 result as the cracking shown in Fig. 7(c) facilitates strut type energy and behaviour. However, FEA results, which do not account for intra-ply cracking, also show good agreement. This is thought to be more coincidental as the large amount of cracking and the consequent displacement of the buckle cannot be captured by the FEA model Inaccurate Plate model predictions may instead be seen to be due to mode-mixity effects which are accounted for in the FEA.

Figure 3 indicates similar variation of threshold strain with sub-laminate stiffness for the results produced by the Plate model and by experimental tests. However, propagation of unbalanced sublaminates with skewed mode shapes is not captured well by the Plate model. This is due to extension-shear coupling (in the 15/30, 15/60, 0/45 and 45/45 sublaminates) which gives rise to a significant Mode II contribution, not fully

represented by the use of a Mode I energy and criterion in the simplifying assumptions of Section 2.1. The bend-twist coupling that is also present in these sublaminates will cause a greater Mode II contribution. Ignoring sublaminates with these features results in predictions that are conservative and within 12% of experimental propagation values.

6. Conclusions

A new Plate model for delamination propagation following sub-laminate buckling has been presented which is accurate to within 12% of experimental results for artificially delaminated laminates with balanced sub-laminate stacking sequences. Intra-ply cracking of surface plies is seen to increase model conservatism. Thus the Plate model offers a simple method for the prediction of compression after impact strength via consideration of 2D strain energy available for propagation. The model is computationally efficient making it suitable for use in optimisation procedures; as such it has potential to bring about a step change in design for damage tolerance in aerospace structures. Such design will lead to improvements in structural efficiency and enhanced product performance.

Acknowledgements

The authors gratefully acknowledge the support of the EPSRC (EP/N024354/1) funding for the ADAPT project. Richard Butler holds the Royal Academy of Engineering - GKN Aerospace Research Chair in Composites Analysis.

References

1. Butler R. Buckling and compressive strength of laminates with optimized fibre-steering and layer stacking for aerospace applications. In: Irving P, Soutis C, editors. Polymer Composites in the Aerospace Industry. Oxford, U. K.: Elsevier, 2014. p. 77-97.

2. Chai H, Babcock CD, Knauss WG. One dimensional modelling of failure in laminated plates by delamination buckling. Int J Solids Struct 1981;17(11):1069–1083.

3. Chai H, Babcock CD. Two-dimensional modelling of compressive failure in delaminated laminates. J Compos Mat 1985;19(1):67-98.

4. Hutchinson JW, Suo Z. Mixed mode cracking in layered materials. Adv Appl Mech 1991;29:63–191.

5. Flanagan G. Two-dimensional delamination growth in composite laminates under compression loading. In: Whitcomb JD, editor. Composite Materials: Testing and Design (ASTM STP 972). Philadelphia: American Society for Testing and Materials, 1988. p. 180-190.

6. Hull D, Shi YB. Damage mechanism characterization in composite damage tolerance investigations. Compos Struct 1993;23(2):99–120.

7. Curtis PT, Gates J, Molyneux CG. Impact damage growth in carbon fibre composites. Technical Report 93009. Farnborough, Hampshire: 1993.

8. Saeed MU, Chen Z, Chen Z, Li B. Compression behavior of laminated composites subjected to damage induced by low velocity impact and drilling. Compos Part B Eng 2014;56:815–820.

9. Sun XC, Hallett SR. Failure mechanisms and damage evolution of laminated composites under compression after impact (CAI): Experimental and numerical study. Compos Part A Appl Sci Manuf 2018;104:41–59.

10. Abir MR, Tay TE, Ridha M, Lee HP. Modelling damage growth in composites subjected to impact and compression after impact. Compos Struct 2017;168:13–25.

11. Tan W, Falzon BG, Chiu LNS, Price M. Predicting low velocity impact damage and Compression-After-Impact (CAI) behaviour of composite laminates. Compos Part A Appl Sci Manuf 2015;71:212–226.

12. Wang J, Wang H, Chen B, Huang H, Liu S. A failure mechanism based model for numerical modeling the compression-after-impact of foam-core sandwich panels. Compos Sci Technol 2017;151:258–267.

13. Melin GL and Schön J. Buckling behaviour and delamination growth in impacted composite specimens under fatigue load: an experimental study. Compos Sci Technol 2001;61(13):1841–1852.

14. Butler R, Rhead AT, Liu W, Kontis N. Compressive strength of delaminated aerospace composites. Philos Trans R Soc A Math Phys Eng Sci 2012;370(1965):1759-1779.

15. Rhead AT, Butler R, Baker N. Analysis and compression testing of laminates optimised for damage tolerance. Appl Compos Mater 2011;18(1):85–100.

16. Baker N, Butler R, York CB. Damage tolerance of fully orthotropic laminates in compression. Compos Sci Technol 2012;72(10):1083–1089.

17. Rhead AT, Butler R, Liu W, Baker N. The influence of surface ply fibre angle on the compressive strength of composite laminates containing delamination. Aeronaut J 2012;116(1186):1315–1330.

18. Kinawy M, Butler R, Hunt GW. Bending strength of delaminated aerospace composites. Philos Trans R Soc A Math Phys Eng Sci 2012;370(1965):1780–1797.

19. Rhead AT, Butler R. Compressive static strength model for impact damaged laminates. Compos Sci Technol 2009;69(14):2301–2307.

20. Whitcomb JD. Analysis of instability-related growth of a through-width delamination. NASA Technical Memorandum 86301, National Aeronautics and Space Administration, Washington, DC, Sept. 1984.

21. Williams FW, Kennedy D, Anderson MS, Butler R. VICONOPT - Program for exact vibration and buckling analysis or design of prismatic plate assemblies. AIAA J 1991;29(11):1927–1928.

22. Thompson JMT, Hunt GW. A general theory of elastic stability. London: Wiley, 1973.

23. Butler R, Williams FW. Optimum buckling design of compression panels using VICONOPT. Struct Optim 1993;6(3):160–165.

24. Liu W, Butler R, Mileham AR, Green AJ. Bilevel optimization and postbuckling of highly strained composite stiffened panels. AIAA J 2006;44(11):2562-2570.

25. Liu W, Butler R, Kim HA. Optimization of composite stiffened panels subject to compression and lateral pressure using a bi-level approach. Struct Multidiscip Optim 2008;36(3):235-245.

26. Kennedy D, Featherston CA. Exact strip analysis and optimum design of aerospace structures. Aeronaut J 2010;114(1158):505–512.

27. Whitney JM. Structural Analysis of Laminated Anisotropic Plates. Lancaster, PA: Technomic Publishing Co. Inc, 1987.

28. Wittrick WH, Williams FW. Buckling and vibration of anisotropic or isotropic plate assemblies under combined loadings. Int J Mech Sci 1974;16(4):209–239.

29. Anderson MS, Williams FW, Wright CJ. Buckling and vibration of any prismatic assembly of shear and compression loaded anisotropic plates with an arbitrary supporting structure. Int J Mech Sci 1983;25(8):585-596.

30. Wittrick WH, Williams FW. A general algorithm for computing natural frequencies of elastic structures. Quart J Mech Appl Math 1971;24(3):263-284.

31. Ilyas M, Lachaud F, Espinosa Ch, Salaün, M. Dynamic delamination of aeronautic structural composites by using cohesive finite elements. In: Proceedings of the 17th International Conference on Composite Materials (ICCM/17), Edinburgh, 27–31 July 2009.

32. Falzon BG, Hawkins SC, Huynh CP, Radjef R, Brown C. An investigation of Mode I and Mode II fracture toughness enhancement using aligned carbon nanotubes forests at the crack interface. Compos Struct 2013;106:65-73.

33. Nilsson K-F, Asp LE, Alpman JE, Nystedt L. Delamination buckling and growth for delaminations at different depths in a slender composite panel. Int J Solids Struct 2001;38(17):3039-3071

34. Prombut P, Michel L, Lachaud F, Barrau JJ. Delamination of multidirectional composite laminates at 0°/ ° ply interfaces. Eng Fract Mech 2006;73(16):2427-2442.

35. Chai H, Knauss WG, Babcock CD. Observation of damage growth in compressively loaded laminates. Exp Mech 1983;23(3):329-337.

Figure 1: Idealised post-buckling and propagation of delaminated plate. (a) Plan view of elliptical delamination of area, A, with potential growth dA. (b) Section B-B of (a).

Figure 2: Buckling mode shape comparison for the 0/45 sub-laminate. Left shows the experimentally observed stable buckling mode shape obtained using a DIC plot of out of plane displacement (w). The superimposed circle represents the boundary of the circular delaminated region. Right is the VICONOPT buckling mode shape for the same case. The crosses indicate VICONOPT point supports that present the extent of the circular delaminated region. Eighteen VICONOPT strips were used, producing nineteen node lines.

Figure 3: Comparison of threshold strain from the Strip [14] and Plate models and experiments for various sub-laminates. Sub-laminates are arranged left to right based on highest to lowest effective axial modulus (A_{11}-A_{12}^2/A_{22}) in the 0° direction. * Intra-ply cracking occurred prior to propagation for these tests, see Figure 7.

Figure 4: Comparison of threshold strain from the FEA [14,17] and experiments for various sub-laminates. Sub-laminates are arranged left to right based on highest to lowest effective axial modulus (A_{11}-A_{12}^2/A_{22}) in the 0° direction. * Intra-ply cracking occurred prior to propagation for these tests, see Figure 7.

Figure 5: Load vs. Strain for four strain gauges on 15/60 sub-laminate. Approximate locations of strain gauges 1 and 3 are indicated in (b); Gauges 2 and 4 are located on the opposite surface to Gauges 1 and 3, respectively. Insets show out-of-plane displacement relative to an unloaded reference state. White circles indicate extent of original Teflon insert.

Figure 6: Load vs. Strain for four strain gauges on 15/30 sub-laminate. Strain gauge locations are indicated on (b); Gauges 2 and 4 are located on the opposite surface to Gauges 1 and 3, respectively. Insets show out-of-plane displacement relative to an unloaded reference state. White circles indicate extent of original Teflon insert.

Figure 7: Intra-ply cracks in the surface ply of sub-laminates: (a) 0_2 at 65kN, (b) 45_2 at 160kN; and (c) 15/30 at 160kN.

Declaration of Interest

Funding: This work was supported by the EPSRC as part of the ADAPT project (EP/N024354/1). Richard Butler is supported by a Royal Academy of Engineering/GKN Aerospace Research Chair in Composites Analysis.